Real time Radar interferometry of ocean surface height

Marc Simard[a] and Ernesto Rodriguez[a]

[a] Jet Propulsion Laboratory/ California Institute of Technology, MS. 300-319, 4800 Oak grove Dr., Pasadena, CA 90068, USA, e-mail: marc.simard@jpl.nasa.gov

ABSTRACT

This paper discusses processing of interferometric signal to measure ocean topography. The method corrects for channel misregistration and geometric decorrelation using estimates of the current Earth geoid scenario. The channel misregistration is caused by slight change in the differential time delay between the signal received at one antenna with respect to the other. This algorithm corrects the misregistration over the entire swath with the Chirp-Z transform which resamples the signals appropriately. Another source of error, the geometric decorrelation (or baseline decorrelation), occurs because the targets within the resolution cell contribute different interferometric phases. In essence, the ground projected wavelengths are different for various look angles which produces a shift of the effective spectrum. This is corrected by shifting the spectra relative to one another and by applying filters to eliminate the non-overlapping part of the spectra. However, the co-registration and the spectral shift require the estimation of the current look and incidence angles. We use the Earth Ellipsoid WGS-84 and the Geoid EGM-96 to estimate the geometric parameters to describe the various viewing scenarios encountered around the Earth Geoid. We finally discuss the implications on the signal processing algorithm.

Keywords: real-time, interferometry, ocean, altimeter

1. INTRODUCTION

This paper describes a processing method to produce interferograms for ocean topography measurement, in particular for the Wide Swath Ocean Altimeter (WSOA).[1] The method includes the Z-transform[2] and the spectral shift[3] to improve interferometric correlation and height measurement accuracy. This algorithm also perfoms near real time updates of various signal processing parameters that depend on the time-varying viewing geometry.

Prati and Rocca[4] (1993) formulate the problem of interferometric spectral shift as the variation $\Delta\theta$ of the off-nadir angle (look angle) acts as a frequency shift between both ends of the baseline. This phenomenon is due to the discrepancies from the various element scatterers within the resolution cell which add incoherently. This means the backscattered signal received from antennas with slightly different viewing geometries contains different spectral components of the ground reflectivity spectrum. In the case of ocean surface interferometry the frequency shift results in a reduction of the interferometric correlation. In other cases, this has positive effects: Prati and Rocca[4] use the resulting increased total bandwidth to successfully improve slant range resolution with repeat pass data sets. Similarly, Gatelli et al.[5] use repeat pass data to improve resolution and build "low noise" interferograms by shifting frequency and band pass filtering. They also propose to improve interferogram formation by means of a tunable interferometric SAR sytems.

To improve correlation, we intentionally shift the frequency spectrums relative to each other such that the projected wave vectors on the ground are identical in both channels.[5] We discuss the expected frequency shift for a configuration similar to WSOA in section 2. This shift introduces frequency bands which do not overlap in both channels, thus producing additional noise. Prati filtering or FIR filter may then be used to reject the parts of the signal which do not overlap in the frequency domain[6] (see Figure 1). However, if one considers the Earth geoid, to correctly point to a 15 km ground range (first pixel for WSOA), the slant range rapidly increases by about 20 km between the equator to the poles as shown in Figure 2. This implies the estimation of the incidence angle, and thus the spectral shift, would be inaccurate by assuming a fixed slant range. Some information about the viewing geometry must be used. We investigate the error due to the WGS84 ellipsoid and the Earth Geopotential Model EGM96 and provide possible solutions in section 3.

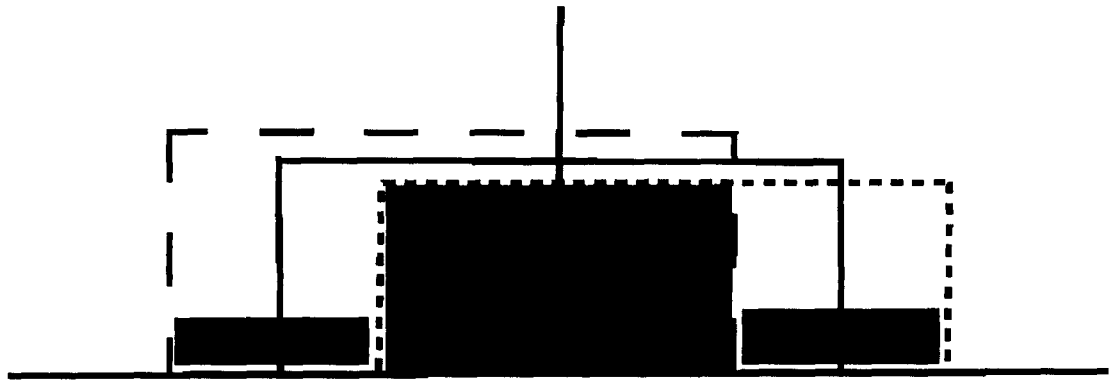

Figure 1. Frequency shift representation. The full line represents the original band spectrum. The FIR filtering isolates the common (or overlapping) part (green) of the spectrums after the individual spectrums are relatively shifted by Δf. The contribution from the non-overlapping bands must be eliminated to reduce noise. The FIR filter specifications relate to the passband (green), the stopband (red) and transition bandwidth which is the separation between the red and green areas.

We design the FIR filter in section 4.1 and assess the effect of error in the estimation of look angle on the interferometric correlation in section 4.2. The frequency shift reduces spatial resolution (section 4.3). In order to apply the proper frequency shift, the incidence angle must be known to a certain degree of accuracy as discussed in section 4.4. Finally the implications of considering changes in the viewing geometry scenario are discussed in section 5

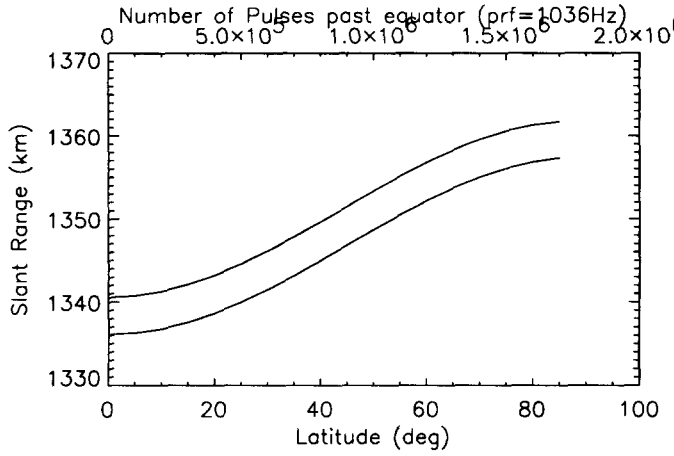

Figure 2. Plot of the variation of Slant Range with latitude. The change of slant range as a function of pulse is also plotted for a pulse repetition frequency of 1036 Hz and a Nodal Period of 6745.76 seconds.

2. SPECTRAL SHIFT ESTIMATION

The frequency shift is given by[4,5]:

$$\Delta f = -\frac{cB_n}{2r_o\lambda tan(\theta - \alpha)} \tag{1}$$

with r_o the distance to the target (Slant Range) and B_n the Baseline component perpendicular to the look direction. We plot the frequency shift as a function of look angle in Figure 3. The shift induced by an error in

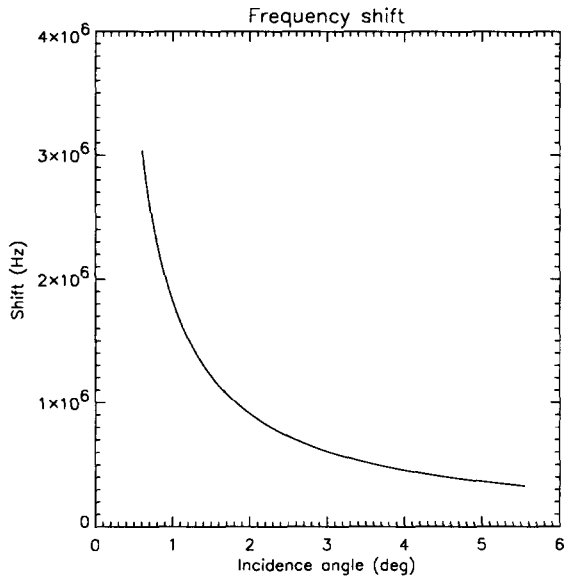

Figure 3. Frequency shift (Δf) as a function of incidence angle θ given by Equation 1.

slant range ∂r is estimated by differentiating Equation 1:

$$\partial(\Delta f) = -\frac{cB_n \partial r}{2r_o^2 \lambda tan(\theta - \alpha)} \tag{2}$$

If $r_o = 1336km$, $B_n = 6.4m$, $f = 13.284E9$ and $\theta = 3.3^o$;

$$\partial \Delta f = 0.412 \cdot \partial r, \tag{3}$$

which is in the order of tens of Hz. The frequency shift error induced by an error in the estimation of θ is much larger than the one introduced by error in r_o. The frequency shift error due to incidence angle error $\partial\theta$ is:

$$\partial \Delta f = -\frac{cB_n}{\lambda 2 r_o} \frac{\partial \theta}{\sin^2(\theta)} = 31796.6 \cdot \frac{\partial \theta}{\sin^2(\theta)}, \tag{4}$$

where $\partial theta$ and θ are in radians. Figure 4 is a plot of the frequency shift as a function of the incidence angle range corresponding to WSOA. The range of incidence angles . Therefore, it is important to find the best estimate of the current incidence angle.

3. THE EARTH IS NOT FLAT NOR SPHERICAL

Let assume the sensor to be at an altitude of 1336km on a polar circular orbit around the Earth Ellipsoid WGS84 with major axis $a = 6378137$ m and minor axis $b = 6356752.3142$ m. The slant range to the 15 km ground range varies as a function of latitude as shown in Figure 2. The resulting incidence angles with respect to the normal to the ground are computed from:

$$\theta_{normal} = arctan(\frac{b^2}{a^2} tan(\theta)). \tag{5}$$

These are plotted in Figure 5 to show the dependence of the incidence angle on latitude.

We go further in our investigation and consider the actual shape of the oceans which is driven by the Earth geopotential. According to the NIMA/NASA Earth Geopotential Model EGM96 (Figure 6),[7] deviation of the Earth geoid from WGS84 are less than ± 100 m. Figure 7 shows examples of height profiles of the EGM96 from latitude -60^o to 60^o. Some example values of look and incidence angles considering EGM96 are also shown

in Table 1. The location at latitude 35^o and longitude 315^oE was chosen because of the large height gradient ($\approx 80cm$) across the instrument swath.

A plot of the effect of a 100 m height deviation from WGS 84 on the estimation of the incidence angle is shown in Figure 8. It can be seen in the figure that the error in the near range is relatively large. Figure 7 shows four EGM96 profiles where the dashed lines represent a linear interpolation using only 5 points. In most cases the slant range error can be reduced significantly while in others the error remains significant. A more accurate interpolation can be obtained with additional points.

4. ANALYSIS OF THE EFFECT OF VIEWING SCENARIO ON THE FIR FILTER METHOD

4.1. Finite Impulse Response filter

This section describes the use of a set of Remez exchange FIR (Finite Impulse Response) filters to correct for the wavenumber shift Δk. Note the FIR filtering occurs after range compression as in Figure 17. The first step in filter design is to identify filter specifications including constraints on the magnitude of the amplitude and phase frequency response. Then one must find the filter coefficients that will produce the acceptable response. The specifications for a realizable low-pass filter will typically be of the form

$$\begin{aligned} 1-\partial_p < |H(e^{j\omega})| \leq 1+\partial_p \qquad & 0 \leq |\omega| \leq \omega_p \\ |H(e^{j\omega})| \leq \partial_s \qquad & \omega_s \leq |\omega| \leq \pi. \end{aligned}$$

These specifications are chosen according to Figure 1 and are defined by the passband off frequency ω_p, the stopband frequency, ω_s, the passband and stopband deviations, ∂_p and ∂_s respectively. The interval $[\omega_p, \omega_s]$ is the transition band. We introduce a set of FIR filters constructed using the Remez exchange algorithm and then analyze their theoretical performance over a unit signal. This algorithm constructs the smallest filter to

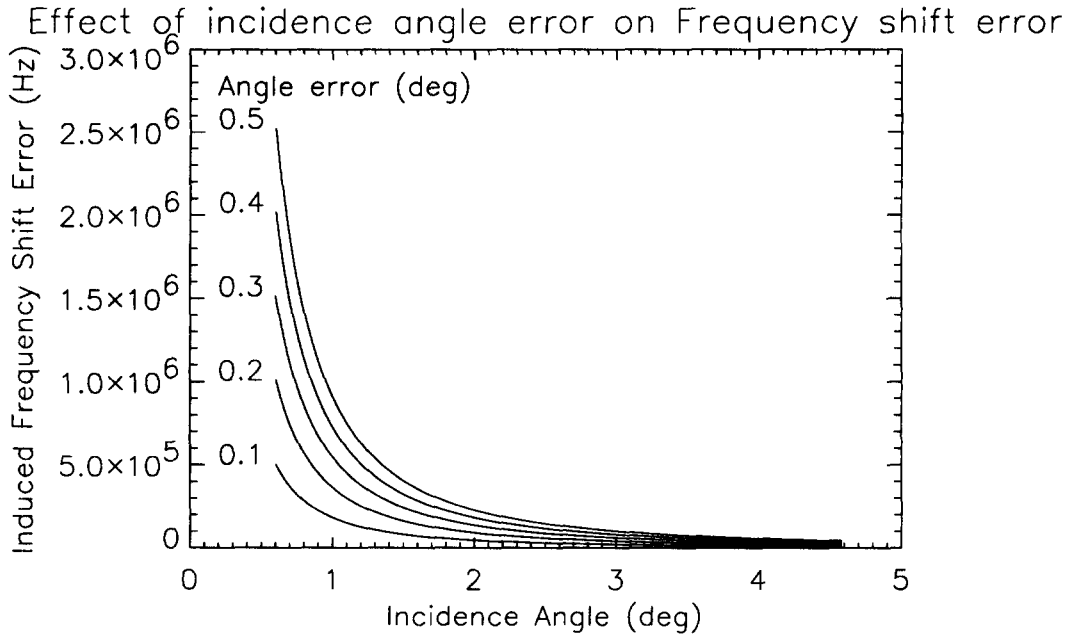

Figure 4. Plot of the expected frequency shift error caused from error in incidence angle estimation. The estimated errors at the equator due to EGM96 vary from 0.38^o at close range and 0.057^o at the far range. Therefore we estimate a maximum error $\partial\Delta f < 2$ MHz in close range and $\partial\Delta f < 0.1$ MHz in mid to far range.

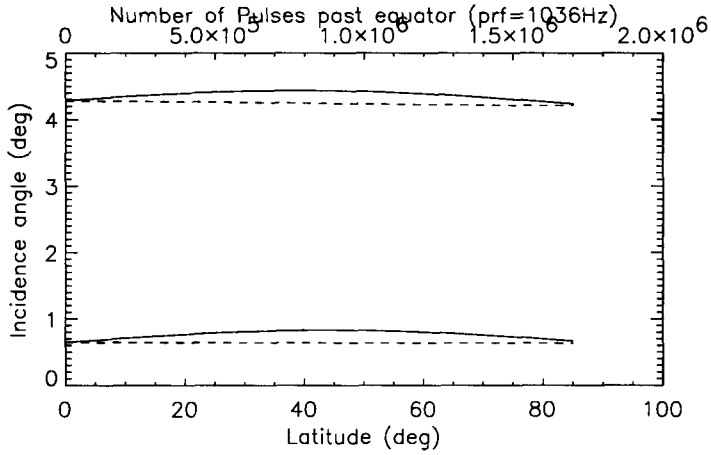

Figure 5. Plot of the variation of incidence angle (full line) with latitude. The change of incidence angle considers the WGS 84 ellipse with a cicular orbit a+1336km. The change is also plotted for a pulse repetition frequency of 1036 Hz and a Nodal Period of 6745.76 seconds. The look angle is also plotted (dash line).

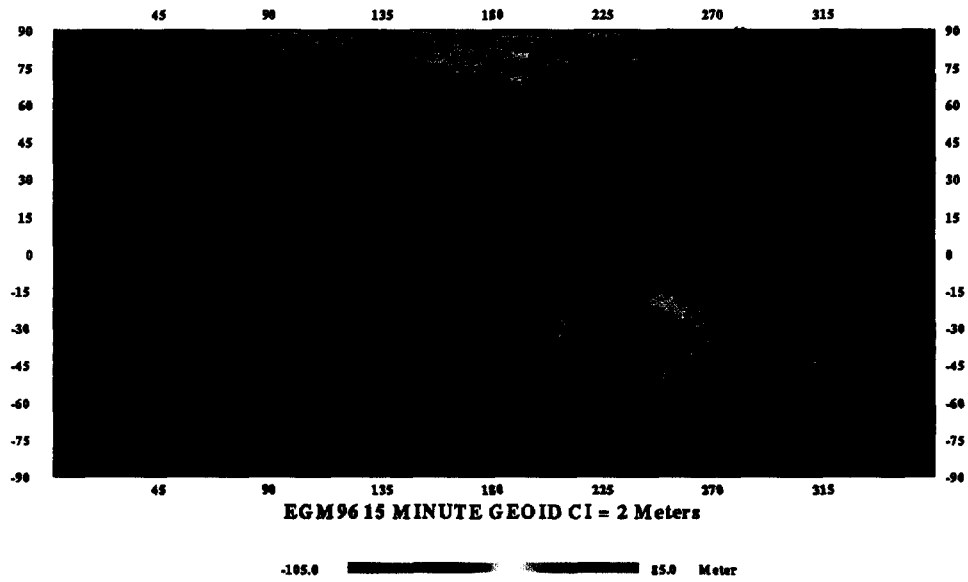

Figure 6. Earth geopotetial Model EGM96.

accomodate given constraints. We constructed a set of filters with various supports (5, 7, 11, 15 and 21 taps) and frequency shifts corresponding to 0.25, 0.30, 0.35, 0.40, 0.4117, 0.45 2π radian cutoff frequencies.

First, we define the filter bandwidth as the $-3dB$ fall off and require the filter passband ripples to be within $1dB$ to preserve signal. We set the transition bandwidth to 0.1 which reduces the passband ripples amplitude to 1dB. These filters do not have an analytical form and their performance is tested numerically. As a reference, Figure 9 shows some examples of FIR filter impulse responses with their frequency response in Figure 10a,b. From the last figure we observe the following:

- large number of taps create small passband band ripples and a deeper stopband;

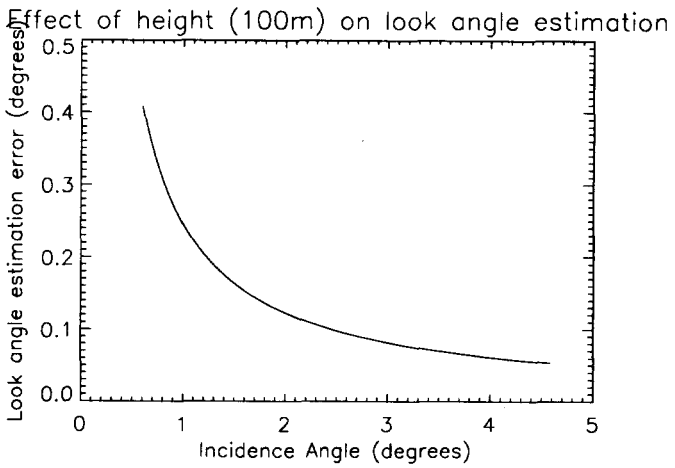

Figure 8. This plot shows the expected estimation error of the look angle for an error of 100 m height. The height error is due to bad interpolation between EGM96 points.

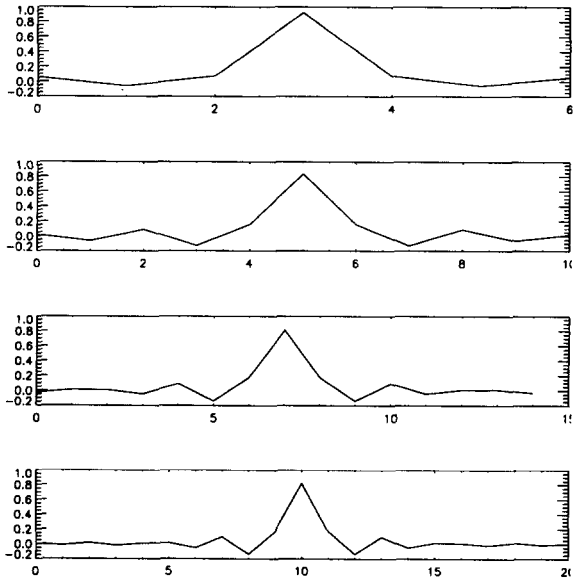

Figure 9. Filter response for 7,11, 15 and 21taps Remez filters.

The standard deviation σ_ϕ of the interferometric phase is given by[8]:

$$\sigma_\phi = \frac{1}{\sqrt{2N_L}} \frac{\sqrt{1-\gamma^2}}{\gamma} \tag{6}$$

where N_L is the number of looks, $\gamma = \gamma_g \gamma_{SNR}$, with the geometric correlation coefficient γ_g and $\gamma_{SNR} = \frac{1}{1+\frac{1}{SNR}} \approx 0.9$. For the purpose of studying the FIR filtering algorithm we only consider γ_g which is computed as:

$$\begin{aligned} \gamma_g &= \frac{| < v_1 v_2^* > |}{\sqrt{< |v_1|^2 >< |v_2|^2 >}} \\ \gamma_g &= \frac{\sum |H(\omega)|^2 W(\omega - \omega_s) W^*(\omega + \omega_s) \partial\omega}{\sum |H(\omega)|^2 |W(\omega)|^2 \partial\omega} \end{aligned} \tag{7}$$

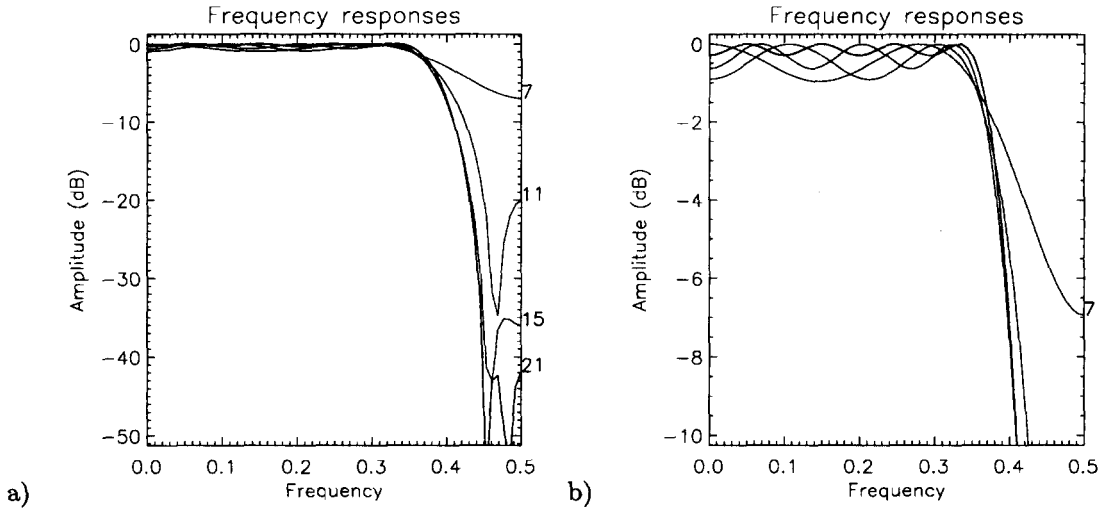

Figure 10. Frequency response of filters with support 21, 15, 11 and 7 with a transition bandwidths 0.1 and cutoff frequency 0.4. Both (a) and (b) show the same filters but emphasizes their differences. Largest filters have deeper stopband (a) and smaller passband ripples (b).

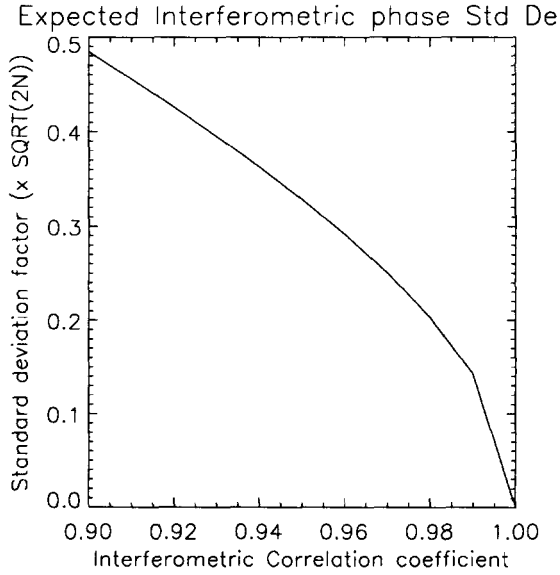

Figure 11. Interferometric phase standard deviation expected from high interferometric correlation between two channels.

Equation 7 results in large variations of the interferometric phase even for very high channel correlation coefficients as shown in the plot of Figure 11. However, this variance is reduced by the number of looks N_L (6).

For the set of filters we obtain average correlation values of 0.8985, 0.916, 0.983, 0.993, 0.993 for 5, 7, 11, 15 and 21 tap filters respectively. More detail on the results are shown in Table 2 with the effect on relative spatial resolution. Using interferometric correlation and resolution from Table 2 in (6), we obtain the result shown in Figure 13. While the unfiltered signal noise decreases linearly with cutoff frequency (which is equivalent to frequency shift), the Remez filters are relatively insensitive to the frequency shift. However, for every frequency shift corresponds a different Remez filter part of a filter bank. We did not represent the 5 tap filter because the passband ripples were large for low frequency shifts. In fact at a frequency shift of 0.4, the 5 tap filters shows a poor stopband near -3dB. On the other hand the 7 tap filter has a stopband of -6dB (see Figure 10a). In Figure 13, we also can observe a maximum improvement using 15 taps. A 15 tap Remez filter provides

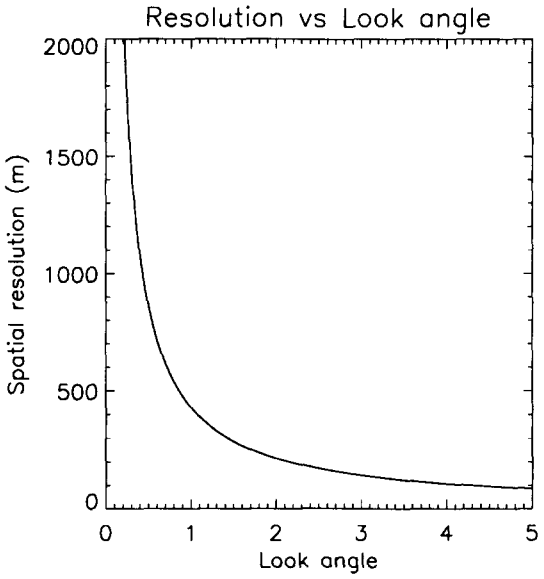

Figure 12. The system intrinsic spatial resolution corresponding to a 20MHz bandwidth. It will be coarser with the FIR filtering as the bandwidth reduces.

passband ripples within $0.5dB$ and stopband of $-40dB$ compared to $1dB$ and $-30dB$ for 11 taps. The height error corresponding to deviation σ_ϕ is given by Rodriguez and Martin[8]:

$$\partial h = \frac{r_o \tan\theta}{kB}\sigma_\phi, \tag{8}$$

and is also expressed in Figure 13 for 100 number of looks.

4.3. Effect of the filtering on the resolution and number of looks

This subsection describes the evaluation of the number of looks considering two factors:

- the signal spatial resolution versus data product resolution;
- the pulse repetition frequency (prf)

For a sensor with a 20MHz bandwidth, the ground spatial resolution follows $\frac{7.5m}{\sin\theta}$ as shown in Figure 12 (e.g. 430m at 1^o and 108m at 4^o). For an acceptable data pixel size of 15km, we can average about 30 range sample points in the near range up to 150 sample points in the far range. At the boresight look angle of 3.3^o, data samples can be averaged to obtain 115 looks. If pulses are considered independent, we estimate 2683 of them on an azimuth distance of 15km leading to more then 300 000 potential number of looks at boresight look angle. This means the height error depicted in Figure 13 is further reduced to 2.2cm and 1.1cm using the 7 and 11 tap FIR filters respectively and using the total available number of looks at boresight angle.

Let assume an altitude of $1334km$ (similar to Jason-1) with a swath from 15 to $100km$ which corresponds to look angles of 0.64423^o to 4.28708^o. Figure 3 is a plot of the theoretical frequency shifts for the configuration of WSOA which shows a significant frequency shift decreasing from near to far range. With a 20MHz bandwidth and 22.5 MHz sampling frequency, the FIR filter cutoff frequency ranges from 0.31854 to 0.42561 from near to far range respectively. Similarly, Figure 14 shows the cutoff frequency as a function of look angle and its effect on spatial resolution. The plot shows the rapid increase of the relative spatial resolution toward its maximum (e.g. 1 relative to the resolution of a full bandwith) with the look angle. Thus near nadir ($\theta \leq 1^o$), low resolution will be achieved if FIR filtering is to occur. The low spatial resolution will also reduce the number of potential looks.

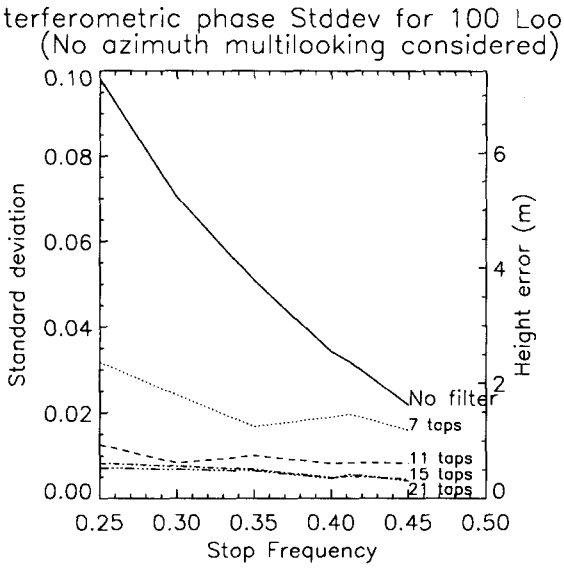

Figure 13. Interferometric phase standard deviation as a function of cutoff frequency (2π) expected from numerical channel correlation of the set of Remez filters (7, 11, 15 and 21 taps). The results are shown for 100 looks. With 2 or 3 order of magnitude larger number of looks, WSOA will have smaller errors. The right axis is the expected height error for 100 looks.

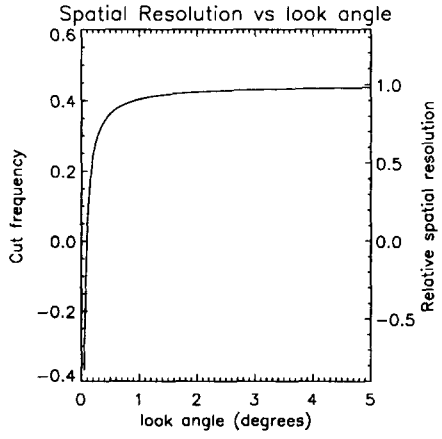

Figure 14. This plot shows the relation between the cutoff frequency and the look angle. Only the band within the cutoff frequency is conserved by FIR filtering, reducing the system bandwidth and thus, the spatial resolution relative to the original system spatial resolution. This plot corresponds to the WSOA configuration with a 20 MHz bandwidth and 22.5MHz sampling frequency. The plot shows the maximum achievable relative resolution, that is using an ideal filter. The spatial resolution using FIR filters are shown in Table 2.

4.4. Effect of the incidence angle estimation error on the FIR filter method

We must now define a tolerance limit on the estimation of the incidence angle for the FIR filters to improve interferometric correlation. Previously, we estimated errors of nearly 0.5^o due lack of knowledge about the spacecraft location with respect to EGM96. The resulting frequency shift error approaches 2 MHz in the near range but rapidly decreases in the far range as shown in Figure 4. In the far range, Figure 8 also shows that the look angle estimation is more accurate and therefore the frequency shift estimation is further improved. Thus, the issue remains more severe in the near range.

Table 2. Interferometric correlation and Resolution: Compare the Remez exchange filters with the unfiltered theoretical interferometric channel

frequency	correlationγ_g	Resolution
No filtering		
0.25	0.508	0.5
0.30	0.6	0.6
0.35	0.692	0.7
0.40	0.8	0.8
0.4117	0.815	0.8234
0.45	0.892	0.9
Remez 5		
0.25	0.864	0.516
0.30	0.897	0.625
0.35	0.850	0.734
0.40	0.872	0.891
0.4117	0.990	N/A
0.45	0.920	N/A
Remez 7		
0.25	0.873	0.516
0.30	0.908	0.609
0.35	0.945	0.703
0.40	0.922	0.812
0.4117	0.916	0.828
0.45	0.934	0.953
Remez 11		
0.25	0.978	0.469
0.30	0.989	0.531
0.35	0.980	0.672
0.40	0.985	0.766
0.4117	0.984	0.797
0.45	0.983	0.859
Remez 15		
0.25	0.991	0.453
0.30	0.990	0.562
0.35	0.991	0.656
0.40	0.994	0.766
0.4117	0.994	0.781
0.45	0.995	0.859

Interferometric correlation was computed using a bank of Remez FIR filters constructed for a series of fixed frequency shifts. Frequency shift errors $\partial(\Delta f)$ were introduced theoritically before computation of the interferometric correlation and its effect is depicted in Figure 15. In the far range the interferometric correlation remains high because $\partial(\Delta f) < 0.1$ MHz. However, in the near range with $\partial(\Delta f) < 2$ MHz the interferometric correlation decrease by almost 0.1.

Figures 16 shows the phase standard deviation computed for 100 looks (i.e. $\sigma_\phi/\sqrt{N_{looks}}$) as well as the resulting interferometric height error for frequency shift errors of 0, 0.4 and 2 MHz. The figures show that for $\partial(\Delta f) < 2$ MHz the interferometric height error is still reduced significantly by the FIR filtering method and the error level is preserved throughout range swath (i.e. frequency shift).

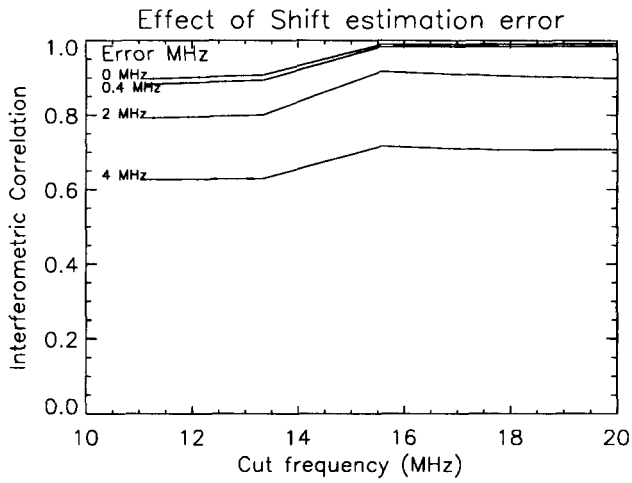

Figure 15. Effect of frequency shift error on the interferometric correlation. The cut frequency is the FIR filter stopband frequency, that is the expected frequency shift. The interferometric correlation is plotted for 4 error levels.

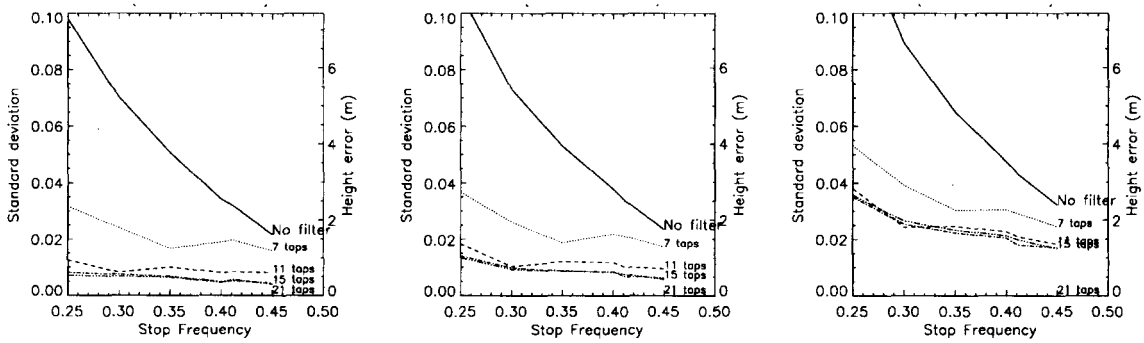

Figure 16. Error induced by frequency shift estimation error of 0.0 MHz, 0.4 MHz and 2 MHz respectively. The phase standard deviation and interferometric height are plotted for 100 number of looks.

5. PROCESSING IMPLICATIONS

The following list shows the main components of the processing steps:

- Parameter initialization and updates to describe current viewing scenarios;
- Down conversion to baseband complex signals I and Q;
- Range misregistration (phasor multiplication);
- Range compression;
- Extraction of swath data (**updated** truncation of rangeline);
- Range misregistration deramp(phasor multiplication) ;
- Frequency shift (phase multiplication);
- Range dependent FIR filtering;
- Interferogram formation (Complex signal multiplication);

- Azimuth block averaging;
- Range block averaging;

The Block diagram of Figure 17 describe the overall algorithm.

5.1. Updates

This processing algorithm is adaptive to the viewing geometry (e.g. look angle θ and time of echo t) which varies with geoid latitude and longitude (viewing scenario). Indeed, phasor parameters must be frequently updated and this update must coincide with the along track averaging boundaries. We use a *scenario table* to initialize the viewing geometry parameters. The *scenario table* contains 512 sets of 4 values ($[t_{dwp}, a_1, a_2, \theta_i]$ described later) representing different viewing geometry scenarios dictated by the the Earth ellipsoid (WGS84) and the Earth geoid (e.g. EGM96) as well as DWP (Data Window Position) time values. Instead of the traditional DWP that specifies the time interval when a radar echo is collected after transmission, a table index I_{DWP} which varies in the range [1,512] indicates the appropriate scenario. A series of 24 indeces I_{DWP} is uploaded to describe one orbit along with their respective duration time Δt_{dwp}. The duration time is translated into a number of averaging boundaries N_{avb} in order to use pulse counters rather then time. Table parameters a_1 and a_2 are the bias and slope of the curve used to estimate the look angle θ. Because the Earth is not flat, we need the 4^{th} value θ_i to translate the look angle θ to the incidence $(\theta + \theta_i)$.

5.2. Update computations

There are various parameters and tables that must be frequently updated using values contained in the *scenario table* by specifying a single I_{DWP} change. Most of the updates involve the computation of the phase z of phasor terms such as e^{iz}. An important array to be computed is $\beta = \frac{1}{2}\frac{\Delta f}{2\dot{T}} \cdot \frac{B \cdot cos(\theta)}{r_i \tan(\theta)}$. The factor $\frac{1}{2}$ is because both interferometric channels will be resampled relative to each other during the processing. The factor $A = \frac{1}{2}\frac{\Delta f}{2\dot{T}} \cdot \frac{B}{r_i}$ is assumed to be a constant and the look angle θ is small such that

$$\beta = \frac{A}{\theta} \tag{9}$$

Note that θ updates are synchronized with the averaging boundaries at rate B_{av} Hz. The fit of θ as a function of slant range is:

$$\theta = a_1 + a_2 * (0.0075 \cdot x)^{0.5}, \tag{10}$$

where $x = [1, 2, ...N_i]$. A typical curve for θ as a function of range as well as its least square fit is shown in Figure 18. The parameters $[a_1, a_2]$ are the values pointed by the I_{DWP}. In particular, a_1 is mainly sensitive to the Earth ellipsoid deviations (e.g. following EGM96) and a_2 mainly depends on the latitude (i.e. Ellipsoid itself). Using the *next* values, we interpolate linearly from the previous I_{DWP} values $[a_{i1}, a_{i2}]$ to these *next* $[a_{f1}, a_{f2}]$ to obtain current $[a_1, a_2]$. The interpolation uses the increment n_{avb} (average boundary count) given the number of averaging boundaries N_{avb} to the next I_{DWP} change.

$$a_1 = a_{i1} + n_{avb}\frac{a_{f1} - a_{i1}}{N_{avb}}. \tag{11}$$

Every update is directly or indirectly related to the number of pulses within one averaging boundary P_{av}.

5.3. Update rate

Let define the averaging boundary to occur at a rate B_{av} Hz which corresponds to averaging an integer number P_{av} of rangelines. The choice of B_{av} is driven by the value of the PRF (e.g. 1036.055 Hz) and the desired ground spatial resolution ($\approx 1\,km$). For example, we desire to average over 1 km ground in the along-track direction and assume the prf of 1036.055 Hz and a ground speed of 5.8 km/s. To obtain the 1 km averaging, we must average $int(\frac{1036.055Hz}{5.8km/s}) \approx 180$ rangelines corresponding to averaging at rate 5.756 Hz.

The table index I_{DWP} actually points to the values that represent the *next* geoid scenario. This is to interpolate from the *past* values to the *next* values at rate B_{av} Hz. The I_{DWP} changes must also be synchronized with the occurrence of the averaging boundary. These updates are when $N_p = P_{av}$ and $N_p = n_{10}$ as well as when the I_{DWP} changes.

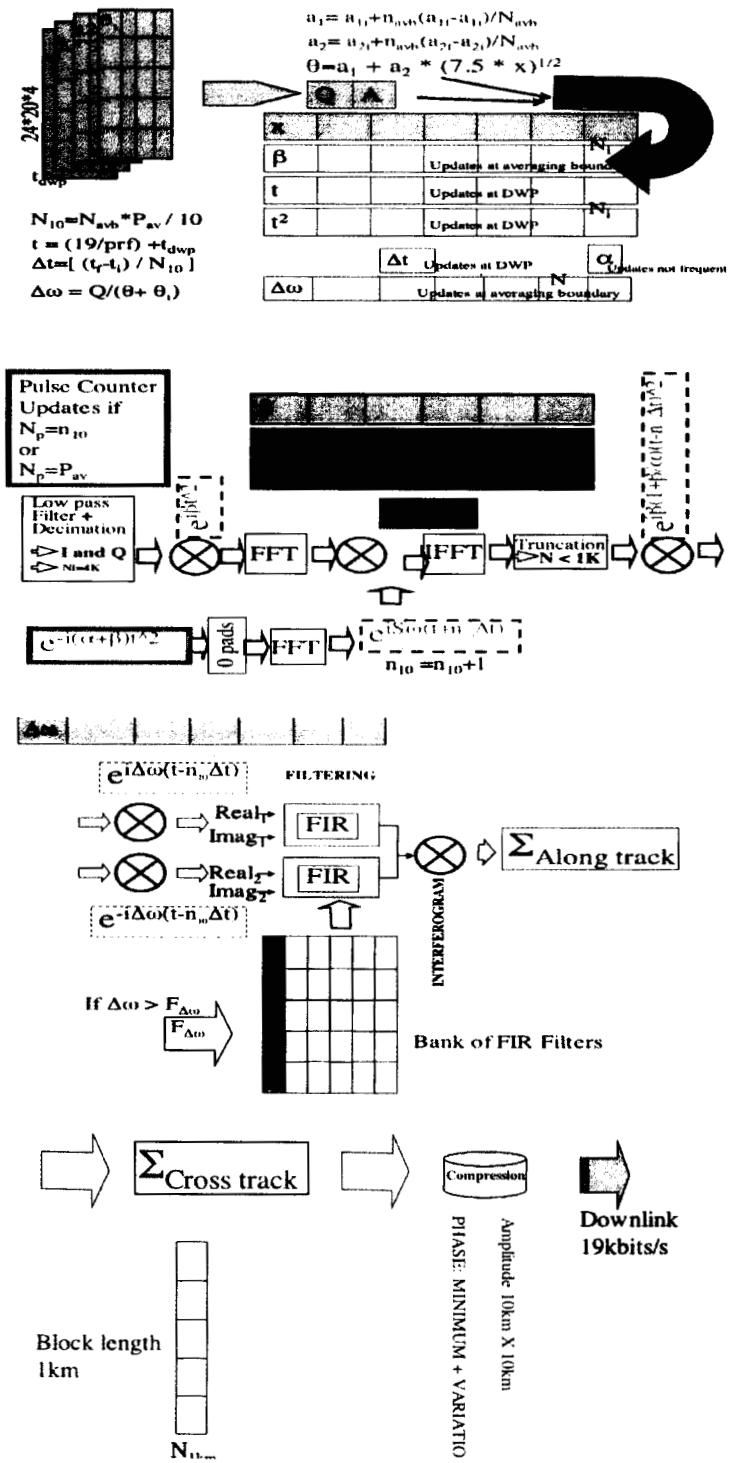

Figure 17. Block digagram describing the Algorithm to construct interferograms.

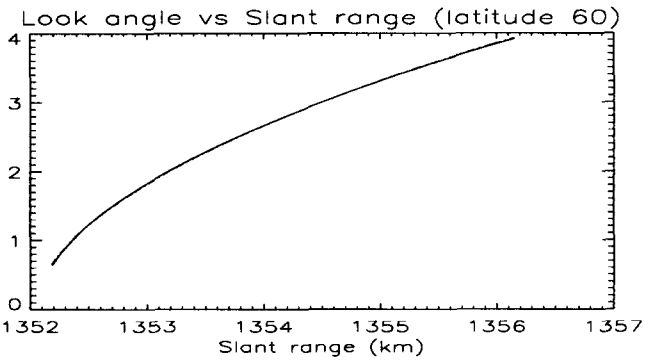

Figure 18. This plot shows the dependence of the look angle on the slant range for WSOA over the Earth ellipsoid WGS-84. The function $\theta = a_1 + a_2 * (r - r_i)^{0.5}$ with $a_1 = -0.0037$, $a_2 = 0.0355$ and $r_i = 1352$ km was fit to the data with $\chi^2 = 0.0066^o$.

5.4. Chirp-Z Transform

The processing algorithm includes a chirp-Z transform. The chirp-Z transform is required to compensate (scale) for the misregistration of signals between the two interferometric channels. The chirp-Z requires only complex multiplies and Fourier transforms. The scaling is dependent on the look angle θ and thus requires updates. The main steps of the chirp-Z transform involve the scaling of the signal in the frequency domain (deramp) prior to range compression; the signal is multiplied by the quadratic phasor $e^{i \cdot \beta \cdot t^2}$. The effect of this phasor is to scale the signal in the frequency domain. The range compression includes a resampling step and a time shift phasor. After the frequency is scaled, the resampling is performed by multiplying the reference function with the phasor $e^{\pm \beta t^2}$ such that

$$e^{-i(\alpha \pm \beta) \cdot t^2}. \tag{12}$$

The effect will be the registration of the interferometric signals in the time domain. The convolution of the reference function of (12) and the signal also involves an additional phasor multiplication which compensates for the variation of slant range with latitude. The actual time of echo (or slant range) to a fixed ground range varies because of the circular orbit around the Earth ellipsoid (note t includes an absolute shift for the current geoid scenario computed relative to both channels). In fact, the slant range to the 15 km ground range may vary up to 3 m between averaging boundaries and as much as 3 km between I_{DWP} changes. If no additional correction is applied, the along-track averaging will be performed over loosely overlapping samples. The change of slant range is considered by updating the timing term $t + n_{10}\Delta t$ of the phasor $e^{\pm i\omega(t + n_{10}\Delta t)}$ which effect is to continuously shift the correct part of the rangeline signal to the first samples (≈ 1000). The parameter ω is the frequency and t and Δt are the current geoid corrected time of echo and the additional time increment respectively. The factor n_{10} increases by 1 every 10 pulses so that the total time $t + n_{10}\Delta t$ increases by Δt every 10 pulses. The complex product of the Fourier transform of the reference function and the shifting term are computed every 10 pulses as:

$$fft(e^{-i(\alpha \pm \beta) \cdot t^2}) \cdot e^{\pm i\omega(t + n_{10}\Delta t)}, \tag{13}$$

where β is updated every average boundary B_{av} Hz and t, t^2 and Δt are updated every change of I_{DWP}.

5.5. phasor multiplication

The effect of the phasor introduced before range compression is removed by multiplying the signal with the phasor $e^{i \cdot \beta \cdot (t - n_{10}\Delta t)^2 (1 \pm \frac{\beta}{\alpha})}$. The parameters β and t^2 are updated. Then, the term $1 \pm \beta/\alpha$ is computed using the table elements corresponding to the truncated range. This phasor also takes into accounts the time shift $t + n_{10}\Delta t$ applied to the reference function such that the appropriate ramp correction is applied to each range sample.

5.6. Frequency shift

The frequency shift is applied to both interferometric channels in the spatial domain by multiplying the signal of one channel with a linear time phase ramp $e^{i\omega t}$ and the other channel with the complex conjugate $e^{-i\omega t}$. The phase shift table $\Delta\omega$ is computed using the incidence angle $\theta + \theta_i$ and a constant value Q such that $\Delta\omega = Q/(\theta + \theta_i)$. Because the frequency shift and the phasor multiplication of section 5.5 may be applied simultaneously, the complex multiplication factor becomes:

$$e^{i\cdot\beta(1\pm\frac{\beta}{\alpha})\cdot(t-n_{10}\Delta t)^2\pm\Delta\omega(t-n_{10}\Delta t)}. \tag{14}$$

The $\pm$ is chosen for the appropriate interferometric channel and swath.

5.7. FIR filtering

Each filter is designed to remove a specific part of the spectrums. The range of incidence angles vary significantly over the geoid, and consequently a large table of filters should be used to takes into account the range of variations of θ_i due to the geoid. The filter is selected from the FIR filter bank accordingly to the frequency shift estimated at a given range.

5.8. Interferogram formation

The interferogram is produced from the complex multiplication of the interferometric channels and are averaged to obtain the final product pixel size (e.g. 1 km). The data averaging comprises the along track averaging and the cross track averaging. As described in section 5.1, the size of the block average in the along track direction is P_{av} rangelines (or pulses). This defines the average boundary rate B_{av}. The average is computed up to the P_{av}^{th} sample resulting in approximately 1 km samples in the along-track direction. The range averaging is range dependent. The spatial resolution ranges from approximately 671 m to 102 m in the near and far range respectively for 100 km swath. Therefore the number of samples to represent a 1 km ground sampling varies as a function of range and requires the block average size to vary as $ceil(1km/R_g)$. These averaging lengths also determine the number of looks N_l as a function of range such that:

$$N_l = P_{av} \cdot ceil(1km/R_g). \tag{15}$$

There is no direct implications on the interferogram formation and averaging.

6. CONCLUSIONS

In this paper, we considered the variation of the incidence angle due to the Earth Geopotential Model EGM96 and reviewed its effect on the formation of interferograms in the case of ocean surface height measurements. When the look angle is near nadir (as is the case of WSOA) the expected frequency shift reaches 3 MHz. This is significant fraction of the total 20 MHz bandwith and will also reduce spatial resolution proportionally. We estimated the potential frequency shift induced by EGM96 to be in the order of 2 MHz in the near range decreasing interferometric correlation by almost 0.1.

To take into account the EGM96, various parameters in the processing algorithms are updated to reflect the current viewing geometry scenario (e.g. incidence angles and range). The update rate is dictated by the product spatial as well as height accuracy requirements. In order to estimate the frequency shift to better then 0.5 MHz, the incidence angle estimate should be better then 0.1^o as shown in Figure 4 which implies the current topography (EGM96) should be estimated within 25 m. Thus, over 10 updates of the I_{DWP} are necessary to estimate EGM96 between latitude -60^o and 60^o. The estimates between updates are obtained from (10) giving the current scenario.

The research described in this paper was carried out at the Jet Propulsion Laboratory, California Institute of Technology, under a contract with the National Aeronautics and Space Administration.

REFERENCES

1. E. Rodriguez, B. Pollard, and ed. D. B. Chelton, "Report of the high resolution ocean topography science working group meeting," *NASA/JPL and Oregon State University* , pp. 190–215, 2001.
2. A. Oppenheim and R. Schafer, *Discrete Time Signal Processing*, Prentice Hall, Englewood Cliffs, NJ, 1989.
3. F. Gatelli, F. Monti-Guarnieri, F. Parizzi, P. Pasquali, C. Prati, and F. Rocca, "The wavenumber shift in SAR interferometry," *IEEE Transactions on Geoscience and Remote Sensing* **4**(32), pp. 855–865, 1994.
4. C. Prati and E. Rocca, "Improving slant-range resolution with multiple SAR surveys," *IEEE Transactions on Aerospace and alectronics systems* **29**(1), pp. 135–143, 1993.
5. F. Gatelli, A. Monti guarnieri, F. Parizzi, P. Pasquali, C. Prati, and F. Rocca, "The wavenumber shift in SAR interferometry," *IEEE Transactions on Geoscience and Remote Sesing* **32**(4), 1994.
6. A. Reigber, "Range dependent spectral filtering for minimize the baseline decorrelation in airborne sar interferometry," *IGARSS'99* , pp. 1721–1723.
7. NIMA/NASA, "Earth geopotential model 96," *www.nima.mil/wgsegm* .
8. E. rodriguez and J. Martin, "Theory and design of interferometric synthetic aperture radars," *IEE Proceedings-F* **139**(2), pp. 147–159, 1992.